Nanomedicine

ISSN: (Print) (Online) Journal homepage: www.tandfonline.com/journals/innm20

Biocompatibility and Proteomic Profiling of DMSA-Coated Iron Nanocubes in a Human Glioblastoma Cell Line

Marina Ulanova, Lucy Gloag, Chul-Kyu Kim, Andre Bongers, Hong Thien Kim Duong, J Justin Gooding, Richard D Tilley, Perminder S Sachdev & Nady Braidy

To cite this article: Marina Ulanova, Lucy Gloag, Chul-Kyu Kim, Andre Bongers, Hong Thien Kim Duong, J Justin Gooding, Richard D Tilley, Perminder S Sachdev & Nady Braidy (2024) Biocompatibility and Proteomic Profiling of DMSA-Coated Iron Nanocubes in a Human Glioblastoma Cell Line, Nanomedicine, 19:4, 303-323, DOI: 10.2217/nnm-2023-0304

To link to this article: https://doi.org/10.2217/nnm-2023-0304

Research Article

For reprint orders, please contact: reprints@futuremedicine.com

Nanomedicine

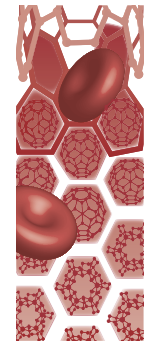

Biocompatibility and proteomic profiling of DMSA-coated iron nanocubes in a human glioblastoma cell line

Marina Ulanova*[,1], Lucy Gloag[2], Chul-Kyu Kim[1], Andre Bongers[3,4,5], Hong Thien Kim Duong[6], J Justin Gooding[6,7], Richard D Tilley[3,6,7], Perminder S Sachdev[1,8] & Nady Braidy[1]

[1]Centre for Healthy Brain Ageing, School of Psychiatry, University of New South Wales, Sydney, New South Wales, 2052, Australia
[2]School of Mathematical & Physical Science, Faculty of Science, University of Technology Sydney, Sydney, New South Wales, 2007, Australia
[3]Mark Wainwright Analytical Centre, University of New South Wales, Sydney, New South Wales, 2052, Australia
[4]Prince of Wales Clinical School, Faculty of Medicine, University of New South Wales, Sydney, New South Wales, 2052, Australia
[5]National Imaging Facility, University of Queensland, St Lucia, Queensland, 4072, Australia
[6]School of Chemistry, University of New South Wales, Sydney, New South Wales, 2052, Australia
[7]Australian Centre for NanoMedicine, University of New South Wales, Sydney, New South Wales, 2052, Australia
[8]Neuropsychiatric Institute, Euroa Centre, Prince of Wales Hospital, Sydney, New South Wales, 2031, Australia
*Author for correspondence: z5151044@zmail.unsw.edu.au

Background: Superparamagnetic iron core iron oxide shell nanocubes have previously shown superior performance in magnetic resonance imaging T2 contrast enhancement compared with spherical nanoparticles. **Methods:** Iron core iron oxide shell nanocubes were synthesized, stabilized with dimercaptosuccinic acid (DMSA-NC) and physicochemically characterized. MRI contrast enhancement and biocompatibility were assessed *in vitro*. **Results:** DMSA-NC showed a transverse relaxivity of 122.59 $mM^{-1} \cdot s^{-1}$ Fe. Treatment with DMSA-NC did not induce cytotoxicity or oxidative stress in U-251 cells, and electron microscopy demonstrated DMSA-NC localization within endosomes and lysosomes in cells following internalization. Global proteomics revealed dysregulation of iron storage, transport, transcription and mRNA processing proteins. **Conclusion:** DMSA-NC is a promising T2 MRI contrast agent which, in this preliminary investigation, demonstrates favorable biocompatibility with an astrocyte cell model.

Plain language summary: MRI is a powerful tool used in the diagnosis of cancer, strokes and other injuries. An MRI scan can be improved with the use of iron oxide nanoparticles, which enhance the contrast of the image. In this study we have developed cube-shaped iron nanoparticles (nanocubes), which have been previously shown to be more effective at inducing contrast. We demonstrated that iron-based nanocubes do not damage or induce stress in cells and work effectively as an MRI contrast agent. We further analyzed how the nanocubes may affect cell functioning by investigating changes to protein levels in the cells. The results of this study are promising steps towards using iron-based nanocubes as a tool to improve the clarity of MRI scans for medical imaging and diagnosis. Future work must determine whether these nanocubes work effectively and safely in an animal model, which is a critical step in progressing to their use in clinical settings.

First draft submitted: 18 October 2023; Accepted for publication: 5 December 2023; Published online: 25 January 2024

Keywords: imaging • iron nanocubes • magnetic resonance imaging • nanomedicine • proteomics

The use of nanomaterials is widespread across numerous fields including sensing [1], catalysis [2], magnetic data recording and biomedicine [3]. Magnetic nanoparticles are particularly valuable in therapeutic and diagnostic applications across many diseases due to their alterable properties and biocompatibility. Superparamagnetic nanoparticles can be used as contrast agents to improve the sensitivity of MRI, a powerful and noninvasive imaging modality with high spatial resolution [4–6], permitting the diagnosis of tumors, strokes and neurodegenerative diseases. Altering

Taylor & Francis
Taylor & Francis Group

nanoparticle shape has a marked effect on the MRI contrast enhancement, and superparamagnetic iron nanocubes have shown relaxivity up to four-times higher than spherical particles [7], rendering them an exciting new tool for imaging.

The magnetic field of an MRI induces a signal from the small magnetic moment in each proton in tissues, while MRI contrast agents interact with hydrogen atoms in tissues and induce signal changes by shortening either their longitudinal relaxation times (T1-contrast agents) or transverse relaxation times (T2-contrast agents). Magnetic nanoparticles produce a local magnetic field and increase the spin–spin or transversal relaxation of nearby protons, resulting in a darkened image in T2 MRI. Increasingly, nanoparticle formulations in different shapes and materials have been developed to improve magnetization values. Nanorods [8] and elongated nanoparticles (~100 nm length) [9] are advantaged by increased cellular uptake and have achieved high transverse relaxivity (r_2 >340 s^{-1} mM^{-1}). Multicore nanoparticles such as nanoflowers [10,11] and nanoclusters benefit from a high surface area-to-volume ratio due to their 'petals' and multiple magnetic cores. For instance, iron oxide nanoflowers modified with polyethylene glycol and a macrocyclic chelator MANOTA for radiolabelling were developed as dual-mode PET/MRI imaging agents with high relaxivity values [12]. Further development is required to achieve uniform size distributions and composition. Cubic-shaped nanoparticles have high magnetic moments, low surface anisotropy and high crystallinity [13–15], which results in higher levels of magnetization than currently approved magnetic nanoformulations. In a study comparing magnetic nanoclusters, nanorods and nanocubes *in vitro*, nanocubes were superior in terms of relaxivity rates and tumor site delivery efficiency [16]. They are also advantageous in a variety of other applications, demonstrating outstanding performance in magnetic hyperthermia treatment and have been employed in noninvasive monitoring of macrophages with a 1.5 T clinical magnetic resonance scanner, targeting tumors and metastases [17].

As well as conferring superior magnetic properties, the shape of the nanocubes alters the way in which they interact with the cellular environment such as their uptake and movement through the cells. It has been well documented that alterations to nanoparticle physical and chemical properties influence their biocompatibility, uptake and efficacy [18,19]. For instance, rod-shaped particles are more readily internalized into the cell nucleus compared with spherical particles, while functionalization of star-shaped particles [18] compared with spherical particles influences the efficiency of their antigen targeting ability. While, on the other hand, spherical nanoparticles show superior biocompatibility compared with other shapes such as rods [20], dendritic structures [21] and wire-shaped nanoparticles [22]. Iron oxide nanocubes have demonstrated varying toxicological effects in different cell types. In HeLa cells, dimercaptosuccinic acid (DMSA)-coated iron oxide nanocubes resulted in decreased cellular viability after incubation for 24, 48 and 72 h, with a reduction of 78% viability after just 48 h at the lowest concentration, as determined by the MTT cell viability assay [23]. Fe_3O_4/Gd_2O_3 nanocubes coated with nontoxic 3,4-dihydroxyhydrocinnamic acid did not reduce the proliferation rate of L929 cells [24]. Zinc and cobalt-doped iron oxide nanocubes caused a decrease in cell viabilities in HeLa cells, while in RAW 264.7 cells, no toxicity was detected at any of the tested concentrations [25]. These differing results, based on cell type, nanoparticle size, coating and composition, necessitate comprehensive evaluations of all emerging nanoformulations for biomedical application.

Disorders of the central nervous system are particularly difficult to treat due to the low permeability of the blood–brain barrier, which prevents therapeutic and diagnostic agents from reaching the brain parenchyma. Due to their biocompatibility and ability to be functionalized with therapeutics and targeting ligands, iron-based nanoparticles are an excellent tool for targeted imaging and drug delivery for diseases within the brain [26] including, Alzheimer's disease [27,28] and Parkinson's disease [29], as well as metastatic brain tumors [30]. As astrocytes are one of the first cell types encountered at the brain–blood interface by intravenously injected agents, it is important to delineate the impact of nanoformulations on this cell type. Astrocytes make up the highest proportion of cells in the central nervous system of mammals, and play essential roles in neurotransmitter transmission, nutrient production for neurons and regulation of endothelial cells, among others. Upon injury to the brain, astrocytes are activated to either protect or induce toxicity to affected neurons in order to shield the neighboring brain tissue. The review by Dai *et al.* summarizes the research investigating the responses of astrocytes to nanomaterials [31]. Upon exposure to nanomaterials, astrocytes exhibit varying responses. Primary rat astrocytes [32] and U-251 glioblastoma cells [28] exposed to DMSA coated iron oxide nanoparticles did not show a reduction in viability, while astrocytes exposed to cobalt and chromium nanoparticles rescued neuronal DNA damage [33]. However, astrocytes have greater sensitivity than neurons to SiO_2 nanoparticles [34], with disturbances in cell morphology and changes to nucleic acids, proteins and lipids, with the principal mechanism of toxicity related to alternations in secondary structures

of protein in astrocytes. Similarly, SH-SY5Y neurons demonstrated more resistance to iron oxide nanoparticle treatment compared with human-cultured astrocytes [35]. Consequently, an astrocytic cell line is a valuable model for evaluating the central nervous system biocompatibility of nanoparticles.

Due to the superior magnetic properties of iron oxide nanocubes, they are a promising material for MRI contrast enhancement. Nanoparticles with high relaxivity values require a lower dose to induce contrast, which reduces the likelihood of side effects or accumulation of the particles in tissues. In this study, we evaluated DMSA-coated iron core iron oxide shell nanocubes (DMSA-NCs) as a novel T2 MRI contrast agent and assessed their stability and biocompatibility in U-251 glioblastoma cells. Transmission electron microscopy (TEM) demonstrated the localization of DMSA-NC within the cells, and proteomics permitted elucidation of the cellular pathways that are altered in response to interaction with the nanoparticles.

Materials & methods

Chemicals & materials

Mesitylene (purity 98%) oleylamine (70%, technical grade), DMSA and triethylamine (purity ≥99.5%) were purchased from Sigma-Aldrich (MO, USA). Toluene (99.5%), hexane (95%) and ethanol were purchased from Chem-Supply Pty Ltd (Gillman, Australia). For *in vitro* experiments, Gibco Roswell Park Memorial Institute (RPMI) 1640 media, trypsin/EDTA (0.25%) and phenol red, lactate dehydrogenase cytotoxicity assay, and protein BCA assay were purchased from Thermo Fisher Scientific (Sydney, Australia), and fetal bovine serum (FBS), L-glutamine and 1% antibiotic/antimycotic were purchased from Sigma-Aldrich. ROS/Superoxide detection kit was sourced from Enzo Life Science (NY, USA). Materials used in experiments pertaining to proteomic analysis were as follows: RIPA lysis buffer (Thermo Fisher Scientific), phenylmethylsulfonyl fluoride (Roche, Sydney, Australia) and trypsin (Promega, Sydney, Australia).

Synthesis of Fe nanocubes

To synthesize the iron seeds, 0.3 g $Fe(C_5H_5)(C_6H_7)$ was dissolved in a solution containing 6 ml mesitylene and 1.5 ml oleylamine. The reaction mixture underwent a 72-h reaction at 130°C with 3 bar of hydrogen. After cooling, the iron seeds were reprocessed in an argon-filled box for further growth. Nanocubes were generated by introducing 1 ml of crude iron seed solution to a mixture of $Fe(C_5H_5)(C_6H_7)$ iron precursor (0.1 g, 0.75 mmol), 6 ml mesitylene and oleylamine (0.5 ml, 0.75 mmol). This process was repeated twice followed another reaction involving 3 ml of the crude iron seed solution in a mixture of $Fe(C_5H_5)(C_6H_7)$ iron precursor (0.3 g, 0.75 mmol), 6 ml mesitylene and oleylamine (0.5 ml, 0.75 mmol). The nanocubes were centrifuged (4000 r.p.m., 30 min), redispersed in toluene at a concentration of 100 mg nanoparticles/ml and subsequently coated with DMSA to permit their dispersibility in water.

DMSA coating of Fe nanocubes

DMSA (50 mg) was added in a centrifuge tube and dissolved in acetone (25 ml). The solution was then sonicated for 5 min. Hexane (50 ml) was added into the DMSA solution and an aliquot of Fe nanocubes solution (0.5 ml) was further added. The DMSA-NC solution was stirred using a vortex for 20 min. Triethylamine (5 ml) was added into the DMSA-NC solution, which was sonicated for 5 min. This previous step was repeated until a total of 250 ml of triethylamine was added into the solution. Milli-Q water (50 ml) and hexane (100 ml) were added into the DMSA-NC solution and the mixture was shaken and allowed to separate into two immiscible layers. The water layer was collected and placed into a clean centrifuge tube. The DMSA-NCs wre centrifuged for 20 min at 10,000 r.p.m. and the black precipitates were collected and redispersed in ethanol (absolute, 50 ml). The DMSA-NCs were again centrifuged for 20 min at 10,000 r.p.m. and the resultant black nanoparticles were redispersed in Milli-Q water for further characterizations.

Characterization of particle size & zeta potential

The hydrodynamic diameter of the DMSA-NCs was assessed in various solutions: Milli-Q water, 1× PBS, RPMI cell media and artificial cerebrospinal fluid (aCSF) using dynamic light scattering (DLS; Malvern Instruments; Zetasizer Nano, Malvern, UK). In addition, the zeta potential of the DMSA-NCs in water was also measured by this instrument. Each sample underwent triplicate measurements at 25°C following a 120-s equilibration period, with an 80-s acquisition time.

For the analysis of size distribution in the dry state, TEM was conducted (Phillips CM200 field emission TEM). Image analysis was conducted using ImageJ [36], with over 100 particles counted to calculate size and size distribution. Dispersion of DMSA-NCs in aCSF was examined using TEM. Artificial CSF solution contained 119 mM NaCl, 26.2 mM $NaHCO_3$, 2.5 mM KCl, 1 mM NaH_2PO_4, 1.3 mM $MgCl_2$, 10 mM glucose and 2.5 mM $CaCl_2$ dissolved in purified water.

MRI of DMSA-NCs

In vitro MRI assessments of DMSA-NCs were conducted as previously described [28] at room temperature (22°C) on a 9.4T Bruker (Karlsruhe, Germany) BioSpec Avance III 94/20 system equipped with a 72-mm internal diameter quadrature radiofrequency coil and BGA-12S HP gradients with maximum strength 660 mT/m and slew rate 4570 T/m/s. Increasing concentrations (0.1, 0.2, 0.5, 1, 100 and 500 µM) of DMSA-NC in Milli-Q water were prepared and Eppendorf tubes containing the solutions were secured in a rack 3D-printed in house for scanning.

A 2D Multi Spin Echo pulse sequence (64 spin echo images in coronal orientation, total echo time range: 10–662 ms) was used for image acquisition for nanoparticle T2 relaxation quantification. The sequence parameters were as follows: TR = 10 000 ms, TE = 10.3 ms, 64 echoes, matrix size = 128 × 128, image in-plane resolution = 0.35 × 0.35 mm, slice thickness = 2 mm, eff. spectral BW = 78125 Hz, total acquisition time with 2 ADC averages: 42 min. Calculation of T2 decay maps was completed by pixelwise fitting of a mono-exponential decay to the echo time image series. Mean T2 relaxation times and 1/T2 relaxation rate (R2 in Hz) were calculated with ROIs over the sample tubes in the images.

Lactate dehydrogenase assay to determine cytotoxicity

Cytotoxicity of the DMSA-NCs was evaluated in U-251 cells (American Type Culture Collection). Cells cultured in RPMI 1640 media supplemented with 10% FBS, 1% L-glutamine, 1% antibiotic/antimycotic at 37°C under a humidified atmosphere of 5% CO_2 as previously described [28], and subsequently seeded onto a flat-bottomed 24-well plate. Prior to treatments, DMSA-NCs were redispersed in solution by vortexing for 20 s followed by brief sonication in a bath sonicator (five sonications of 3 s duration, with 5-s breaks). Cells were exposed for 24 h at 37°C to varying concentrations of DMSA-NC (0.1 µM-500 µM). Negative blank control cells were left untreated. All samples were treated in triplicate. At the conclusion of the 24-h incubation, cell supernatants were collected and cells underwent three washes with 1× PBS. Subsequently, 200 µl of 1× PBS was added to each well and sonicated for 30 s with a probe sonicator to homogenize the cells. The LDH content of the supernatant was measured using an LDH cytotoxicity assay. Protein level was detected using a Protein BCA assay kit and used for normalization of the LDH measurements.

Determination of reactive oxygen species/superoxide production

A total reactive oxygen species (ROS) detection kit was used to investigate the production of ROS/superoxide in U-251 cells following treatment by DMSA-NC. Cells were seeded onto 96-well plates with black walls and incubated overnight at 37°C. Cells were exposed to three concentrations of DMSA-NC for 24 h. Each concentration was replicated in six wells. After the incubation, the solution in each well was aspirated. ROS/superoxide detection reagent (100 µl) was pipetted into each well, and the plate was placed into an incubator at 37°C for 30 min. Fluorescence readings were taken on a plate reader for fluorescein (total ROS; excitation/emission = 488 nm/520 nm) and rhodamine (superoxide; excitation/emission = 550 nm/610 nm).

DMSA-NC internalization into cells

Internalization protocols were used as described in [28]. Briefly, to investigate the amount of iron taken up by cells during a 24 h of treatment, U-251 cells were incubated with DMSA-NC (5 µg iron). After 24 h, the supernatant from each well was collected and cells were washed using 1× PBS three times. Wash solutions were combined with the supernatant to prevent loss of nanoparticles that had detached from the surface of cells. Subsequently, each well was filled with 200 µl 1× PBS and cell homogenization was achieved through 30-s probe sonication. Homogenized cells and supernatants were submitted with ICP-MS evaluation of iron concentration.

Separately, U-251 cells were seeded onto coverslips for analysis of the intracellular localization of DMSA-NC by TEM. Cells were grown until they reached 70% confluency and treated with DMSA-NC (100 µM) for different durations. After 5 min, 1, 6 and 24 h, the cells were fixed with 2% glutaraldehyde and 2% paraformaldehyde (24 h, 4°C). The coverslips with the fixed cells were then washed in 0.1 M sodium phosphate buffer (pH 7.4)

prior to postfixation in 2% OsO_4 in 0.1 M sodium phosphate buffer (60 min, 4°C). Increasing concentrations of ethanol were then used to dehydrate the samples. Subsequently, Procure 812 resin was used to infiltrate the samples, followed by polymerization at 60°C for 48 h. The samples were sectioned at 70 nm using a Leica EM UC6 Ultramicrotome and collected onto carbon-coated copper mesh grids. Uranyl acetate and lead citrate was used for poststaining. Images were taken on a Jeol JEM 1400 electron microscope (accelerating voltage 100 kV).

Proteomics analysis of U-251 cells treated with DMSA-NC

Cell culture & DMSA-NC treatment

Treatments for proteomics and sample preparation were conducted as described previously [28]. U-251 cells were seeded onto T25 flasks and treated with a 100-µM concentration of DMSA-NC once they had reached 80% confluency. Following a 24-h incubation at normal growth conditions, the media was replaced with fresh unsupplemented media, then cells were collected using a cell scraper. Washes were conducted by pelleting the cells by centrifugation for 5 min (500 × g, ambient temperature). Following aspiration of the media, the cells were resuspended in 1× PBS. This was repeated three times. After the last wash, 200 µl of 1× PBS was added to the vials, which were placed into -80°C freezers until further analysis.

Cell lysis & protein digestion

RIPA lysis buffer containing protease inhibitor, 0.1 mM phenylmethylsulfonyl fluoride, was used to resuspend cells treated with DMSA-NC after they had thawed. Disruption of cells was carried out with probe sonication (5 × 5–10-s bursts). Between each sonication, the cells were briefly chilled on ice. Protein cysteine disulphides reduction was carried out at 60°C for 60 min in 2 mM tris(2-carboxyethyl)phosphine (TCEP), followed by the addition of iodoacetamide for 10 min, ambient temperature for cysteine alkylation. Subsequently, elimination of nonprotein components including detergents, reducing and alkylating agents was achieved by the addition of 1 ml of cold acetone containing 1% HCl to each sample. For protein precipitation, samples were placed in a -20°C freezer for 12–14 h, then pelleted by centrifugation at 13,000 r.p.m. for 20 min (ambient temperature). Following removal of the supernatant, the pellets were briefly air dried, then a lysis buffer containing 5% SDS and 100 mM ammonium bicarbonate (pH 7.5) was added to the samples. S-Trap Mini spin traps (Protifi, NY, USA) were used to capture and desalt proteins following the manufacturer instructions. Proteins were digested overnight at 37°C in 1 µg sequencing-grade trypsin in 50 mM ammonium bicarbonate (100 µl), which was added to each sample in the traps. Peptides were eluted from the S-trap by sequentially adding 100 µl each of 0.2% formic acid and 50% acetonitrile containing 0.2% formic acid, then centrifugation at 4000 r.p.m. for 2 min, ambient temperature, at each step. All the elutions were pooled and dried under vacuum centrifugation (SpeedVac, Thermo Fisher Scientific). After drying, 50 µl of 1% formic acid containing 0.2% heptafluorobutyric acid was added to the tubes to resuspend the peptides. A microspectrophotometer (DeNovix, DE, USA) was used to estimate protein concentration (absorbance = 280 nm, mg/ml protein determined using the extinction coefficient of albumin).

Tandem mass spectrometry & database searching

For each set of biological triplicates, analysis was performed using the Q-Exactive Plus mass spectrometer (Thermo Electron, Bremen, Germany) connected to a nano-LC, Dionex UltiMate 3000 high-performance liquid chromatography system (Thermo Fisher Scientific, MA, USA), and equipped with an autosampler (Dionex, Amsterdam, The Netherlands). The mass spectrometer parameters for data-dependent acquisition analysis and nano-LC conditions that were used in this study have been described [28,37]. Peptides (~3 µg on-column) were first captured onto a C18 cartridge (Acclaim PepMap 100, 5 µm 100 Å, Thermo Fisher Scientific Dionex), and subsequently switched to a capillary column (25 cm length, 350 µm o.d., 75 µm i.d.) that contained reverse-phase packing (C18, Reprosil-Pur, 1.9 µm, 200 Å, Dr. Maisch GmbH, Ammerbuch-Entringen, Germany). The elution of peptides was achieved over a 60-min run time and a binary gradient of 0–45% buffer B at 200 nl/min. The buffers were as follows: buffer A (H_2O/CH_3CN of 98:2 containing 0.1% formic acid) and buffer B (H_2O/CH_3CN of 20:80 containing 0.1% formic acid). The following mass spectrometer settings were used: ion-spray voltage 2000 V, capillary temperature 300°C, positive ion mode, survey scan acquired (m/z 375–1750) and up to ten multiply charged ions (charge state ≥2+) isolated for MS–MS fragmentation.

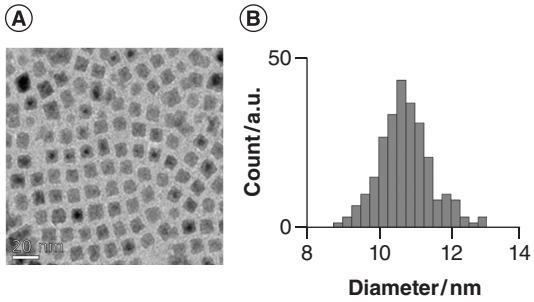

Figure 1. The physicochemical properties of DMSA-coated iron core iron oxide shell nanocubes. (A) Transmission electron microscope image of DMSA-coated iron core iron oxide shell nanocubes (DMSA-NC), demonstrating the cubic shape of the nanoparticles. **(B)** Dry diameter distribution of DMSA-NCs, measured in >100 particles using ImageJ software.

Table 1. The hydrodynamic sizes of DMSA-coated iron core iron oxide shell nanocubes in different solutions.

LM6	Milli-Q water	1× PBS	aCSF	RPMI media
Z-average (nm)	159.8	74.88	1505	168.1
PdI	0.178	0.197	0.519	0.305
RSD (%)	0.231	4.36	5.2	1.51

aCSF: Artificial cerebrospinal fluid; PBS: Phosphate-buffered saline; PdI: Polydispersity index; RSD: Relative standard deviation.

Bioinformatics

The raw files from the LC-MS/MS were searched against the Uniprot human complete database downloaded 2022.08.30 using MaxQuant v2.1.3.0 (downloaded from www.maxquant.org). LFQ was employed as label-free quantification method and the minimum ratio count was set to 2 and minimum number of neighbors to 3. All further identification and quantification parameters were set as default.

Downstream statistical processing was performed on the Perseus computational platform version 2.0.6.0 (downloaded from www.maxquant.org/perseus) [38]. Raw intensity values were filtered by columns: 'Only identified by site', 'Reverse', and 'Potential contaminant' to exclude false–positive hits. The filtered values log2-transformed and the features not reaching 100% valid values in at least one group (each comparison) were filtered out. After that, missing values were replaced from normal distribution (width 0.3 and down shift 1.8). Differentially expressed protein between groups were analyzed with the student *t*-test to calculate the p-value.

The differentially expressed proteins (foldchange >1.2 or <0.8; $p < 0.05$) were used to analyze functional enrichment. Gene ontology analysis of biological processes, molecular function and cellular components was conducted using the Database for Annotation, Visualization and Integrated Discovery (DAVID; https://david.ncifcrf.gov/) and visualized using GraphPad PRISM 9. Gene Ontology analyses use 'gene product' to refer to genes and any structures encoded by the gene, i.e., proteins. Reactome pathway were analyzed with 'clusterProfiler' [39] and 'ReactomePA' [40] R software packages and visualize the result with the 'enrichplot' R software package. Protein–protein interaction analysis of the identified differentially expressed proteins was employed using STRING version 11.5 (http://string-db.org) [41].

Statistical analyses

The mean and standard deviation (SD) for all experiments are expressed as mean ± SD. Statistical analysis was performed by ANOVA followed by Tukey's multiple comparisons *post hoc* test (for three groups or more) or student's *t*-test (between two groups). Significance was assigned at $p < 0.05$. Data were analyzed using GraphPad Prism 8.4.3 (GraphPad Software, CA, USA).

Results

DMSA-NC characterization

The iron nanocubes were characterized with high-resolution TEM to obtain selected area electron diffraction to confirm the formation of Fe cube nanoparticles. From the selected area electron diffraction, the patterns produced by the nanoparticles matched iron and iron oxide crystal structures, hence confirming the presence of Fe nanocubes in the samples. This was previously reported in [42]. The DMSA-NCs had a cubic shape and a dry diameter of 10.7 nm ± 0.9 nm (Figure 1). The hydrodynamic sizes of the nanoparticles were 159.8, 74.88, 1505 and 168.1 nm in water, 1× PBS, aCSF and RPMI cell media, respectively (Table 1). The surface of the DMSA-NCs was negatively charged with a zeta potential of -26.7 ± 6.27 mV. Due to the large hydrodynamic size measurement

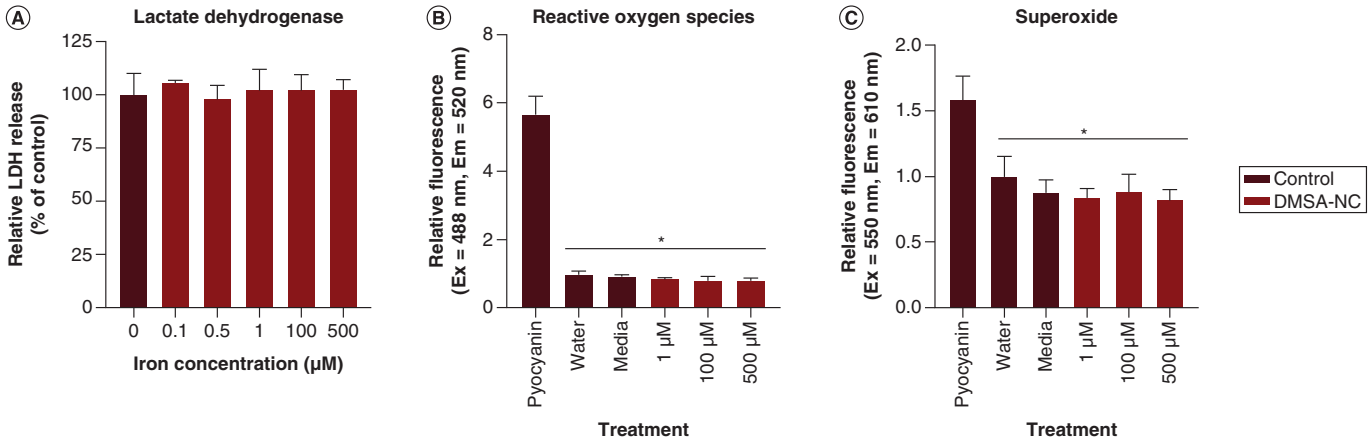

Figure 2. DMSA-coated iron core iron oxide shell nanocubes show biocompatibility in U-251 cells. (A) Lactate dehydrogenase release relative to control wells treated with Milli-Q was not significantly increased in U-251 cells, following 24-h incubation with increasing concentrations. Data represent mean ± standard deviation (n = 3). Statistical analysis was carried out using one-way ANOVA. **(B)** Reactive oxygen species (ROS) and **(C)** superoxide production did not increase in cells following 24-h incubation with DMSA-NC at all three evaluated concentrations. Generation of ROS and superoxide in control and DMSA-NC-treated wells were significantly lower than cells treated with a ROS inducer (pyocyanin) used as a positive control. Control wells were treated with Milli-Q water. Data represent mean relative fluorescence intensity to the water measurement ± standard deviation (n = 6). One-way ANOVA with Tukey's multiple comparison's test *post hoc* test was performed.
*Significant difference from positive control; $p < 0.05$.
DMSA-NC: Dimercaptosuccinic acid-coated iron core iron oxide shell nanocube.

of DMSA-NCs dispersed in aCSF, these particles were imaged using TEM to determine whether aggregation had occurred (Supplementary Figure 1). The images show the salts present in the aCSF and DMSA-NCs well dispersed in the salt matrix, with nanoparticle diameters corresponding to the measured dry diameter, demonstrating the stability of the DMSA-NCs in aCSF. Furthermore, the solution was purified by filtration to remove the interference in the image from the salts. Qualitatively, the particles were observed close together but not aggregated.

Cell viability & ROS/superoxide production

Exposing the cells to increasing concentrations of DMSA-NC was shown not to be detrimental to cell viability. LDH is a marker of damage to the plasma membrane, as upon breakage it is released from the cell into the cytoplasm. No increase in LDH was detected at any of the concentrations relative to control (Figure 2A). Oxidative stress is one of the ways in which nanomaterials induce toxicity in cells. No increases in ROS production or superoxide were observed in the cells following the addition of DMSA-NC, even at concentrations up to 500 μM (Figure 2B & C).

DMSA-NC internalization into U-251 cells

Uptake of DMSA-NCs in U-251 cells was determined by ICP-MS, followed by TEM imaging to investigate the distribution of the nanoparticles within cells. U-251 cells were incubated with a total of 5 μg iron and following 24 h approximately 95% of DMSA-NC were internalized. For the cellular localization experiments, cells were incubated with 100 μM of DMSA-NC for 5 min, 6 h and 24 h, then fixed and visualized using TEM (Figure 3). Agglomerates of nanoparticles near cell membrane protrusions can be observed within 5 min of incubation, as well as inside endosomes and an autophagosome. At 1 h post-treatment, DMSA-NCs have entered endosomes and lysosomes. DMSA-NCs are also observed in multivesicular bodies at 6 h post-treatment and within lysosomes, which suggests their transport through the cell degradation pathway. Mitochondria and nuclei are visible in the micrographs, devoid of DMSA-NCs, and no DMSA-NCs are observed unencapsulated in the cytoplasm. In addition, organelle morphology appears normal, with no obvious changes induced by the presence of DMSA-NC. Interestingly, at 5 min DMSA-NC were observed to agglomerate in a ring formation in the endosomes (Figure 3A, inset, arrowhead).

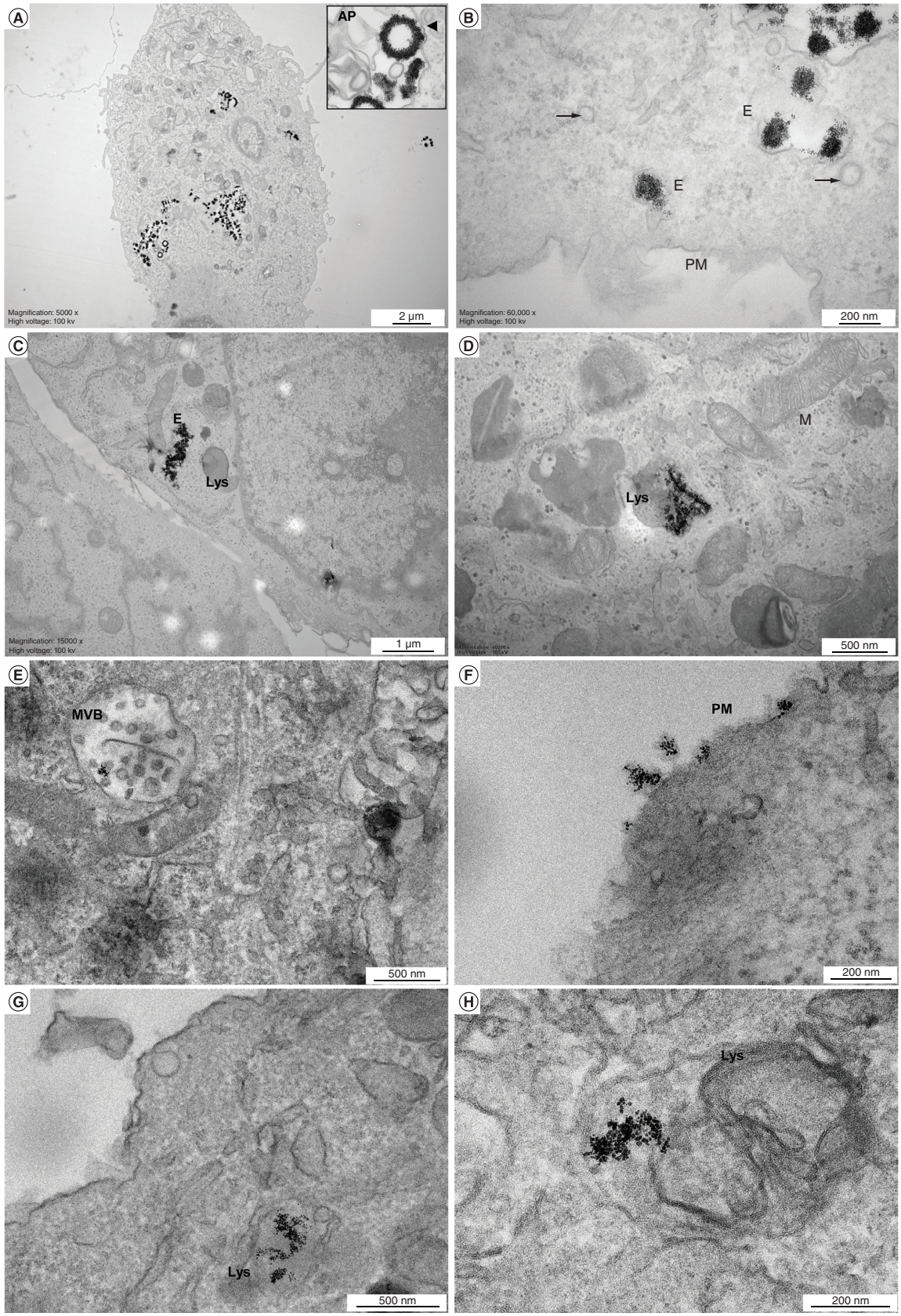

Figure 3. Transmission electron microscope analysis of DMSA-coated iron core iron oxide shell nanocube internalization into U-251 cells over 24 h of incubation. Cells were incubated with 100 µM of DMSA-NC in RPMI medium at 37°C. Cells were collected for fixation and processing for transmission electron microscope imaging at **(A & B)** 5 min, **(C & D)** 1 h, **(E & F)** 6 h and **(G & H)** 24 h following treatment.
AP: Autophagosome; ER: Endoplasmic reticulum; Lys: Lysosome; M: Mitochondrion; MVB: Multivesicular body; PM: Plasma membrane.

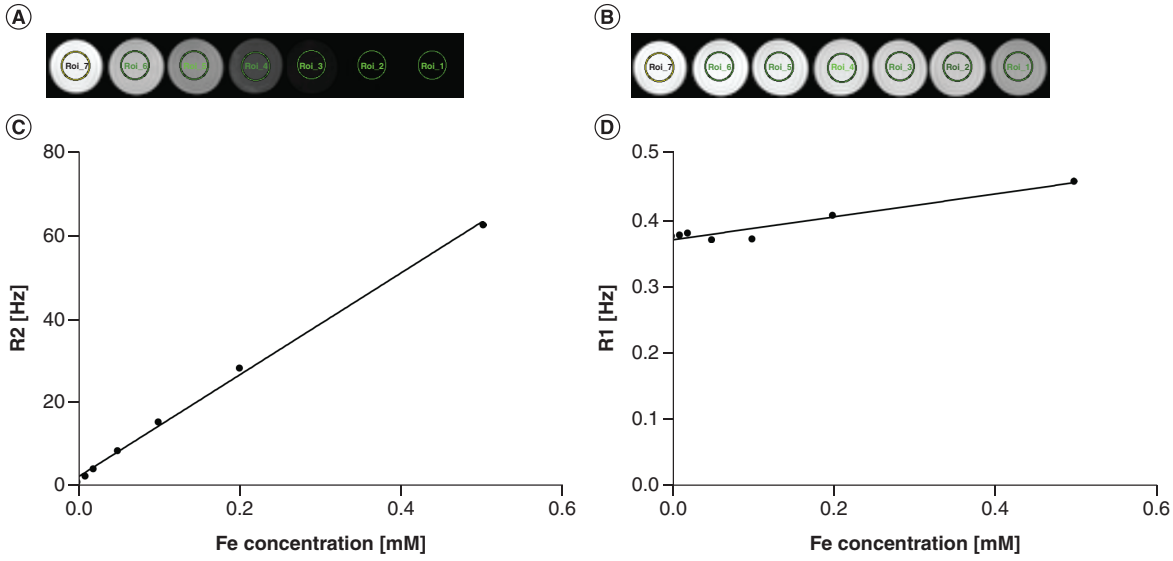

Figure 4. ***In vitro*** **magnetic resonance imaging properties and relaxometry of DMSA-coated iron core iron oxide shell nanocubes. (A)** T2 and **(B)** T1 magnetic resonance imaging of DMSA-coated iron core iron oxide shell nanocubes dispersed in Milli-Q at concentrations of 0, 0.01, 0.02, 0.05 and 0.2 mM Fe (left to right). The inverse curves of **(C)** T2 (R2) and **(D)** T1 (R1) versus concentration where gradient gives the r_2 and r_1 relaxivity, respectively, in mM Fe^{-1}, s^{-1}.

MRI of DMSA-NCs

A concentration gradient of DMSA-NCs was imaged by MRI to evaluate the transverse T2 relaxation and longitudinal T1 relaxation times at 9.4 T. Higher concentrations of DMSA-NCs resulted in darker scans at T2 (Figure 4A). The relaxivities were as follows: r_2 = 122.59 Hz/mM and r_1 = 0.1697 Hz/mM.

Proteomic analysis of U-251 cells after DMSA-NC exposure

Proteomic analysis was undertaken on whole-cell homogenates of U-251 cells following treatment of cells with 100 µM DMSA-NCs or no treatment for 24 h (three replicate incubations under each condition). Untreated cells were used as control cells. A list of all deregulated proteins can be found in Supplementary Table 1. Figure 5 shows the differentially expressed proteins in these comparison groups, and the 20 most significant differentially expressed proteins. Compared with the untreated cells, a total of 99 proteins were differentially expressed, including 56 upregulated and 43 downregulated.

Gene ontology & Reactome

The functional enrichment of gene ontology terms of the 92 differentially expressed proteins was analyzed using DAVID online software [43,44]. Up- and down-regulated proteins were analyzed separately, and proteins were classified according to their biological roles, molecular function and cellular compartment (Figure 6 & Supplementary Table 2).

Gene ontology of biological processes revealed that proteins involved in RNA splicing (RBM39, SF3B3, SF3A2, THRAP3, U2AF1, SRSF4, SRRM1), cytoplasmic translation (RPS26, RPS27, RPL34, RPLP0, RPL13A, RPS24), translation (RPS26, MRPS17, RPS27, RPL34, MRPS23, RPLP0, RPL13A, MRPL28, RPS24), mRNA processing (RBM39, KHDRBS1, SF3A2, THRAP3, SRSF1, HNRNPA2B1, U2AF1, SRSF4, SRRM1) and mRNA splicing, via spliceosome (SF3B3, SF3A2, SRSF1, HNRNPA2B1, HNRNPU, U2AF1, PRPF40A, SRSF4, PLRG1, SNRPC, SNRNP200, SRRM1), were deregulated.

In terms of molecular function, binding functions including RNA binding (KHDRBS1, DAZAP1, DNMT1, RPL34, SRSF1, RPLP0, HMGB3, HNRNPU, U2AF1, YBX3, FBL, FIP1L1, PSMD4, TCOF1, MYO18A, EXOSC3, RAE1, RBM39, CPSF7, SF3A2, MRPS23, MRPL28, RPL13A, NAP1L1, PRPF40A, SRRM1, RPS26, RPS27, THRAP3, SARNP, SUB1, HNRNPA2B1, SRSF4, CEBPZ, SLIRP, CALR, SNRPC, SNRNP200, RPS24, LUC7L2), protein binding (MRPS17, ARF4, DAZAP1, TRAM1, RPL34, PDCD6, RPLP0, HMGB3, HNRNPU, TXNDC12, SMC3, AP2A2, YBX3, HK1, FBL, PSMD4, FTH1, PSMD3, MYO18A, FLOT1, RCC1,

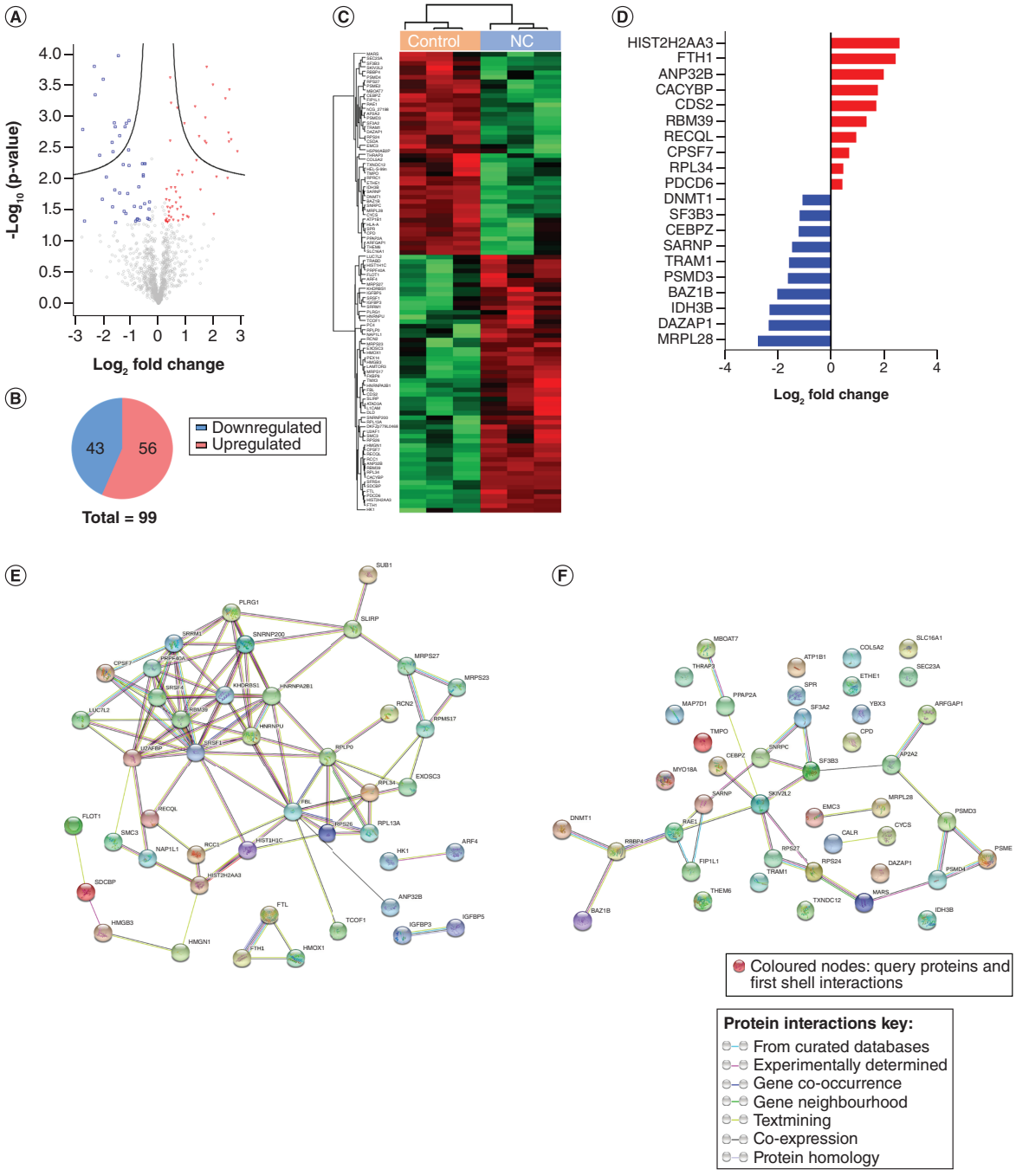

Figure 5. Protein expression in U-251 cells following treatment with DMSA-NC. (A) Volcano plot showing the differentially expressed proteins (DEPs) caused by DMSA-coated iron core iron oxide shell nanocube exposure. All DEPs (FC >1.2 or <0.8; $p < 0.05$) are represented as red dots (upregulated proteins) and blue dots (downregulated proteins). **(B)** Venn diagram illustrating the number of upregulated and downregulated proteins following DMSA-NC treatment compared with control. **(C)** A heatmap depicting the DEPs (FC >1.2 or <0.8; $p < 0.05$) between the two groups of samples using hierarchical clustering. **(D)** The fold-changes of the ten most significantly upregulated DEPs and the ten most significantly downregulated DEPs. **(E–F)** The protein–protein interaction networks of the **(E)** up and **(F)** downregulated proteins in U-251 cells following DMSA-NC treatment compared with control cells analyzed using the STRING database. Each node represents a protein, and the colored lines represent the known or predicted protein–protein interactions.
DMSA-NC: Dimercaptosuccinic acid-coated iron core iron oxide shell nanocube.

Taylor & Francis
Taylor & Francis Group

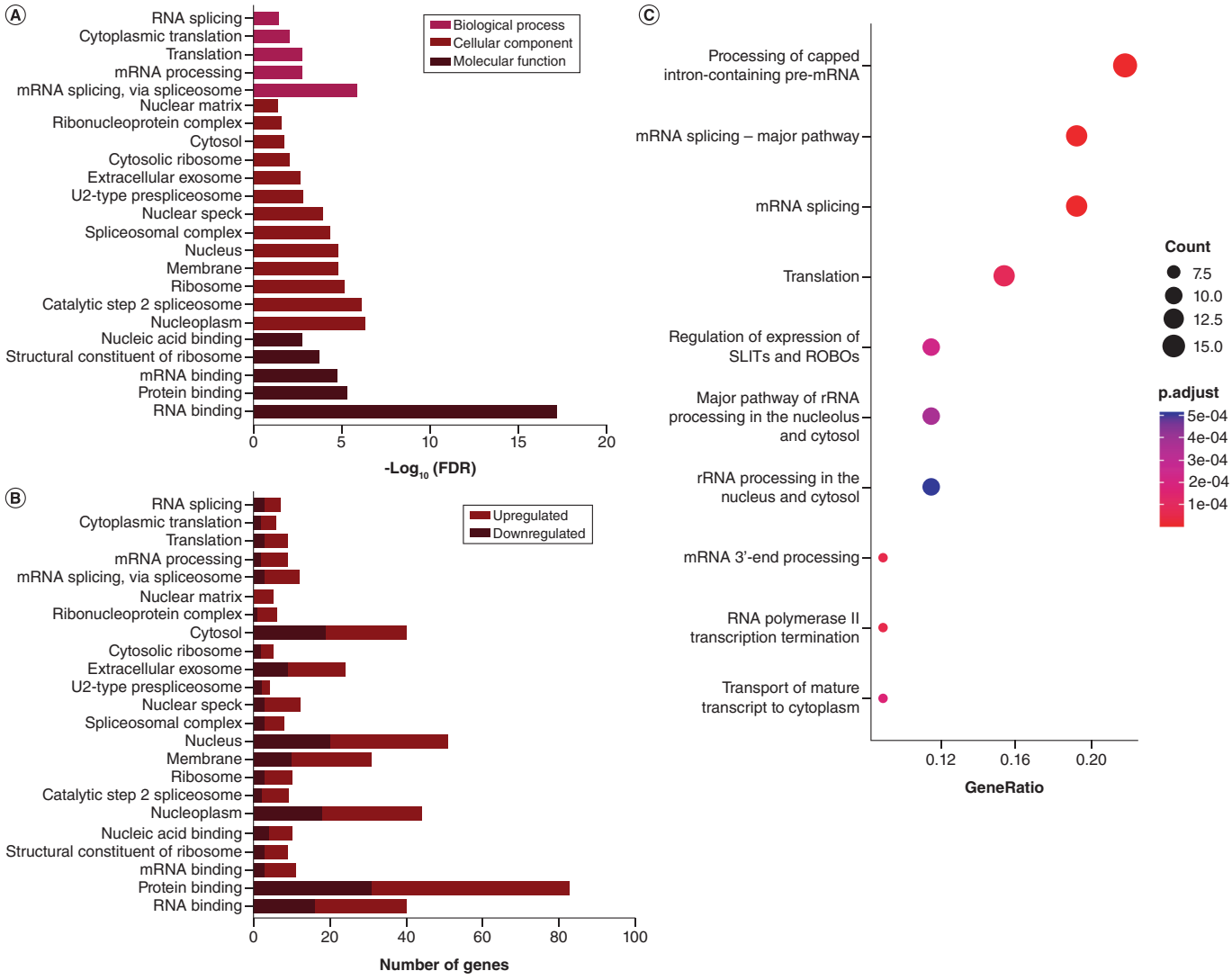

Figure 6. Gene ontology and pathway-enrichment analysis of deregulated proteins by exposure to DMSA-coated iron core iron oxide shell nanocubes in U-251 cells. (A) Enriched gene ontology terms for biological processes, cellular components and molecular functions for deregulated proteins, ordered by p-value (FDR). **(B)** Enriched gene ontology from **(A)** showing the number of up- and down-regulated proteins for each term. **(C)** Top ten significant Reactome pathways from enrichment analysis using differentially expressed proteins. The size of dots represents the count of enriched proteins, and the color of the dots represents the Benjamini–Hochberg adjusted p-values.

TMPO, HMGN1, MRPS27, IGFBP5, IGFBP3, MRPS23, RECQL, CACYBP, PRPF40A, PLRG1, BAZ1B, ATP1B1, ATAD3A, ARFGAP1, SRRM1, RCN2, TMX3, PRKAR1A, THRAP3, SUB1, ETHE1, SARNP, FKBP8, PSME2, SRSF4, SNRPC, SNRNP200, DLD, LUC7L2, FTL, KHDRBS1, SEC23A, DNMT1, SF3B3, SRSF1, U2AF1, SDCBP, TCOF1, RBBP4, FIP1L1, EMC3, HMOX1, EXOSC3, RAE1, rRBM39, CPSF7, SLC16A1, SF3A2, MBOAT7, MRPL28, NAP1L1, L1CAM, PEX14, RPS26, RPS27, HNRNPA2B1, CYCS, CALR, ANP32B, SLIRP, LAMTOR3, CDS2), mRNA binding (RPS26, KHDRBS1, DAZAP1, CPSF7, SRSF1, RPL13A, SRSF4, SLIRP, CALR, SNRPC, LUC7L2) and nucleic acid binding (RBM39, DAZAP1, CPSF7, SF3B3, SF3A2, RECQL, SRSF4, SLIRP, SNRNP200, YBX3) were deregulated. In addition, deregulated were proteins involved in the structural constituent of the ribosome (RPS26, MRPS17, RPS27, RPL34, MRPS23, RPLP0, RPL13A, MRPL28, RPS24).

In response to DMSA-NC treatment, nuclear proteins (nucleoplasm: KHDRBS1, DAZAP1, DNMT1, SF3B3, PDCD6, SRSF1, HNRNPU, U2AF1, SMC3, FBL, SDCBP, FIP1L1, PSMD4, TCOF1, RBBP4, SPR, PSMD3, RCC1, HMOX1, EXOSC3, RAE1, HMGN1, RBM39, CPSF7, SF3A2, RECQL, CACYBP, PRPF40A, PLRG1, BAZ1B, SRRM1, RPS26, RPS27, THRAP3, SARNP, SUB1, ETHE1, HNRNPA2B1, PSME2, SRSF4, ANP32B,

SNRPC, SNRNP200, RPS24 nucleus: DAZAP1, PDCD6, RPLP0, HMGB3, HNRNPU, SMC3, YBX3, FBL, PSMD4, FTH1, PSMD3, MYO18A, IDH3B, RCC1, TMPO, HMGN1, IGFBP3, RECQL, RPL13A, CACYBP, PLRG1, SRRM1, THRAP3, SUB1, SARNP, SRSF4, SNRPC, SNRNP200, DLD, KHDRBS1, DNMT1, SF3B3, SRSF1, SDCBP, RBBP4, HMOX1, EXOSC3, RAE1, RBM39, CPSF7, SF3A2, NAP1L1, PEX14, RPS27, HNRNPA2B1, CYCS, CEBPZ, CALR, ANP32B, SLIRP, RPS24, nuclear speck: RBM39, SF3A2, THRAP3, SARNP, SRSF1, HNRNPU, U2AF1, PRPF40A, SRSF4, PLRG1, LUC7L2, SRRM1, nuclear matrix: HNRNPA2B1, HNRNPU, PRPF40A, SMC3, SRRM1), ribosomal proteins (ribosome: RPS26, MRPS17, MRPS27, RPS27, RPL34, MRPS23, RPLP0, RPL13A, MRPL28, RPS24, cytosolic ribosome: RPS27, RPL34, RPLP0, RPL13A, RPS24), membrane proteins (KHDRBS1, ARF4, RPLP0, HNRNPU, FBL, SDCBP, PSMD3, MYO18A, FLOT1, HMOX1, TMPO, CPSF7, SLC16A1, MBOAT7, RECQL, RPL13A, NAP1L1, PRPF40A, ATP1B1, PEX14, RPS26, PRKAR1A, CPD, HNRNPA2B1, FKBP8, PSME2, CALR, SNRNP200, RPS24, FTL, CDS2), proteins involved in the spliceosome (catalytic step 2 spliceosome: SF3B3, SF3A2, SRSF1, HNRNPA2B1, HNRNPU, U2AF1, PLRG1, SNRNP200, SRRM1, spliceosomal complex: SF3B3, SF3A2, HNRNPA2B1, U2AF1, PLRG1, SNRPC, SNRNP200, SRRM1, U2-type prespliceosome: SF3A2, PRPF40A, SNRPC, LUC7L2), extracellular exosome (HSP90AB2P, ARF4, SLC16A1, PDCD6, RPL34, RPLP0, CACYBP, ATP1B1, RPS26, FBL, SDCBP, SPR, THRAP3, SUB1, CPD, FTH1, PSMD3, HNRNPA2B1, FLOT1, PSME2, CALR, ANP32B, LAMTOR3, FTL), cytosol proteins (HSP90AB2P, KHDRBS1, ARF4, DAZAP1, SEC23A, RPL34, PDCD6, RPLP0, HNRNPU, SMC3, YBX3, AP2A2, HK1, SDCBP, FIP1L1, PSMD4, TCOF1, RBBP4, SPR, FTH1, PSMD3, HMOX1, EXOSC3, TMPO, MRPL28, RPL13A, CACYBP, PEX14, ARFGAP1, SRRM1, RPS26, RPS27, PRKAR1A, MAP7D1, FKBP8, PSME2, CYCS, CALR, RPS24, FTL) and ribonucleoprotein complex (DAZAP1, HNRNPA2B1, RPLP0, RPL13A, HNRNPU, SLIRP) were deregulated.

Enrichment analysis using differentially expressed proteins of Reactome pathways are represented in Figure 6C (Supplementary Table 3). The top ten significant Reactome pathways were determined to be processing of capped intron-containing pre-mRNA ($p < 0.0001$), mRNA splicing – major pathway ($p < 0.0001$), mRNA splicing ($p < 0.0001$), translation ($p < 0.0001$), regulation and suppression of SLITs, and ROBOs ($p < 0.0001$), major pathway of rRNA processing in the nucleoulus and cytosol ($p < 0.0001$), rRNA processing in the nucleus and cytosol ($p < 0.0001$), mRNA 3′-end processing ($p < 0.0001$), RNA polymerase II transcription termination ($p < 0.0001$), transport of mature transcript to cytoplasm ($p < 0.0001$). In addition, further associations were discovered using semantic similarity analysis as confirmation and supplementary information (Supplementary Figure 2). The top 30 significantly altered Reactome pathways were associated with eukaryotic decay (nonsense-mediated mRNA decay) acid, metabolism by acid derivatives, rRNA nucleus cytosol nucleolus, transport mature 3′-end transcript and splicing capped pathway pre-mRNA.

Discussion

We developed DMSA-coated nanocubes that effectively induce T2 MRI contrast enhancement and characterized their biocompatibility in a glioblastoma cell line using cell toxicity assays, TEM and proteomics (Figure 7). Taken together, these results contribute to the current state of knowledge of the cellular response to DMSA-coated nanoparticles and the influence of the shape of the core. Magnetic nanomaterials increase MRI sensitivity and can therefore improve diagnosis of various diseases including cancer and neurodegenerative illnesses.

Colloidal stability and low toxicity are required for biomedical applications of nanomaterials. Previously, studies have shown that magnetic nanoparticles increase in size in suspension because of the formation of aggregates in solution or the attachment of ions and proteins present in the solution to the particle coating [45]. In this study, the DLS-measured hydrodynamic diameter of DMSA-NC was smallest in 1× PBS, had a small increase in size in distilled water and cell media, and was the highest when suspended in aCSF. TEM imaging of DMSA-NC dispersed in aCSF showed DMSA-NC to be distributed throughout the salt matrix with no aggregation, and DLS analyses of aCSF alone showed a peak of approximately 800 nm (not shown). In solutions containing salt or other compounds, DLS favors larger particles, which interfere with the nanoparticle readout. Furthermore, when nanoparticles are exposed to cell media, the proteins present in the media form a protein corona on the surface of the particles. The composition of this corona is determined by the nanoparticle's physical properties as well as the composition of the biological media. For instance, silver nanoparticles incubated in complete Dulbecco's Modified Eagle Medium containing FBS for only 1 h bound to 45–85 different proteins [46]. The dynamics and constituents of protein coronas require further characterization as they impact cell internalization, toxicity mechanisms, can improve

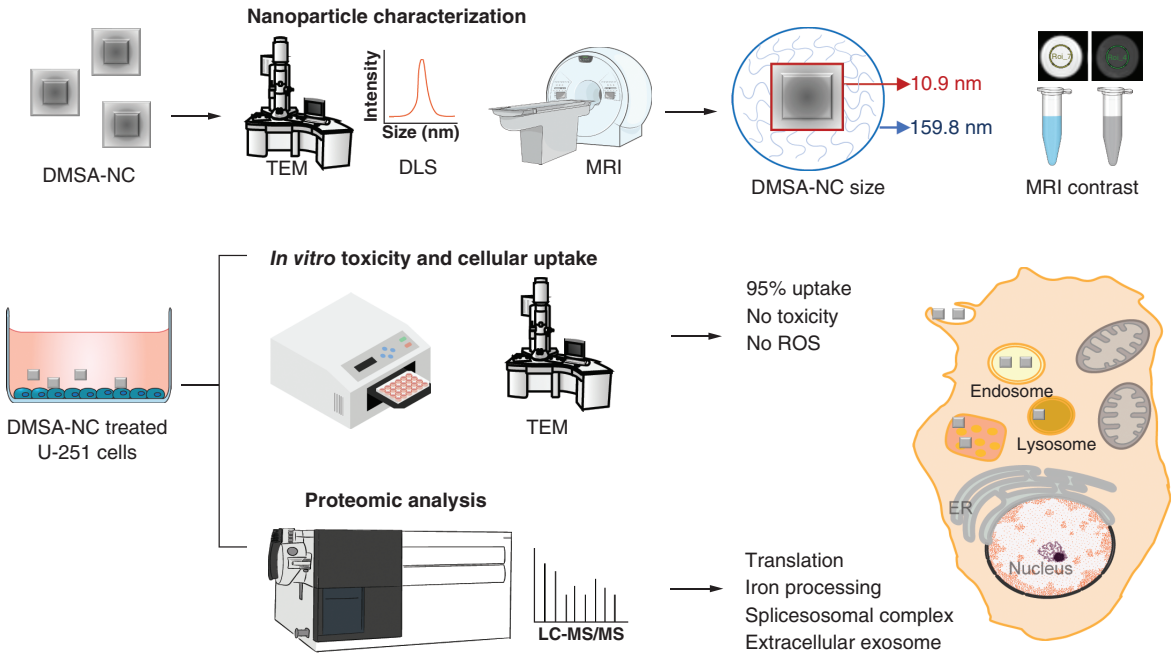

Figure 7. Schematic representation of the study. The generated DMSA-coated iron core iron oxide shell nanocubes (DMSA-NCs) were first characterized using transmission electron microscopy, dynamic light scattering and magnetic resonance imaging to determine the shape, size and relaxivity of the nanoparticles. Subsequently, U-251 cells were treated with DMSA-NCs for *in vitro* assessment of cytotoxicity, cellular internalization of the nanoparticles and proteomics analysis. The *in vitro* studies showed no cytotoxicity, almost total nanoparticle internalization within 24 h and the DMSA-NC localization within cell organelles. Proteomics determined that among other pathways, proteins involved in translation, iron processing and extracellular exosomes were deregulated.
Parts of the figure were drawn using images from Servier Medical Art. Servier Medical Art by Servier is licensed under a Creative Commons Attribution 3.0 Unported License (https://creativecommons.org/licenses/by/3.0/).
DLS: Dynamic light scattering; DMSA-NC: Dimercaptosuccinic acid-coated iron core iron oxide shell nanocube; LC-MS/MS: Liquid chromatography with tandem mass spectrometry; ROS: Reactive oxygen species; TEM: Transmission electron microscopy.

particle stability by preventing agglomeration of particles due to increased steric hindrance [47] alter elimination rates, and in addition can influence their relaxivity [48].

The present DMSA-NCs demonstrated excellent MRI contrast enhancement, with an *r2* relaxivity of 122.59 $mM^{-1}s^{-1}$ at 9.4 T. Previous efforts focused on manipulating shape and size to increase saturation magnetization have determined that nanocubes consistently outperform other configurations [49,50]. Recently developed dual-mode contrast agents can induce T1 and T2 relaxation effects by doping iron oxide nanocubes with other paramagnetic metals, and therefore enhance diagnostic accuracy. Highly monodisperse and crystalline 9.7-nm magnetite nanocubes were synthesized for T1- and T2-weighted MRI showing *r*1 and *r*2 relaxivities of 5.23 $mM^{-1}\cdot s^{-1}$ and 89.68 $mM^{-1}\cdot s^{-1}$, respectively, at 3 T [51]. Zinc-cobalt ferrite nanocubes were evaluated in MRI, MPI and for magnetic hyperthermia treatment [52], and dual-mode Fe_3O_4/Gd_2O_3 nanocubes from T1–T2 dual-mode MRI with $r_1 = 67.57 \pm 6.2$ $mM^{-1}\cdot s^{-1}$ and $r_2 = 24.2 \pm 1.46$ $mM^{-1}\cdot s^{-1}$ [24].

We investigated the *in vitro* biocompatibility of DMSA-NCs using the U-251 glioma cell line as a cell model. Following 24-h incubation, the cells internalized approximately 95% of DMSA-NCs. Previous studies have shown that incubation and uptake of iron oxide nanoparticles by various cells can affect cell viability, including in microglial [53], Alexander, Huh7 and HepG2 cells [54], when treated at high doses of 50 µg/ml. In our study, cell viability in response to DMSA-NCs was determined by evaluating LDH release following 24-h treatment with the nanocubes and no significant differences in LDH release were observed. Furthermore, DMSA-NCs did not cause oxidative stress in cells, as ROS and superoxide production were not significantly impacted.

Electron microscopy showed that DMSA-NCs clustered around the periphery of the cell prior to being engulfed in membrane extensions, suggesting macropinocytosis as the endocytic mechanism. Additional evidence for a clathrin-independent route of internalization was the presence of coated vesicles devoid of DMSA-NCs visible near

the periphery of the cell. Within 5 min of incubation, DMSA-NCs could be observed within an autophagosome as well as in clusters in endosomes, lysosomes and multivesicular bodies during the other time points. The electron microscopy results suggest the involvement of either the lysosome-degradation pathway or the journey of the DMSA-NC to exocytosis. Similarly, Sedra *et al.* found that amine-functionalized iron oxide nanoparticles were localized in multivesicular bodies, then incorporated into the membrane vesicles in the intracellular region and efficiently secreted from the cells 6 days after intracellular delivery [55]. Interestingly, some DMSA-NCs could be observed clustering in ring formations. Although this is outside the scope of the present study, the magnetic interaction in closed ring-shape clusters under a magnetic field can increase the thermal effect of magnetic hyperthermia therapy [56]. In recent years, nanocubes have been extensively researched for magnetic hyperthermia applications in cancer treatment and tumor ablation due to the exceptional heating efficiency, or specific absorption rates, of nanocubes. As such, the observed tendency of the present DMSA-NCs to form rings within cellular organelles could be exploited for enhanced magnetic hyperthermia treatments.

A discovery proteomics approach was conducted to further elucidate the cellular response to DMSA-NCs in this study and determine what cellular pathways are perturbed following their treatment. The cells were treated at a dose of 100 μM iron (35.5 μg Fe) to a confluent T-25 flask of cells, which at confluency has a cell density of 2.8×10^6 cells. Following treatment with DMSA-NC, deregulation of proteins predominantly involved in the translation machinery, influencing mRNA splicing and RNA binding, was observed. The alteration to these mechanisms suggests that internalization of DMSA-NCs causes cells to modify their structure and adjust protein expression by varying DNA and RNA replication processes. Gene ontology and Reactome pathway analysis showed that proteins involved in the composition and regulation of the spliceosomal complex and pre-mRNA processing, as well as ribosomal proteins and translation pathways, were altered. Furthermore, iron storage and processing proteins were expectedly altered following treatment with DMSA-NCs.

The intracellular ferritin complex is composed of FTH1 and FTL, which play a key role in iron metabolism and maintenance of iron homeostasis in cells. In accordance with previous work using iron oxide nanoparticles [57,58], DMSA-NC treatment resulted in an upregulation of both these proteins. Ferritin plays an important role in iron storage and homeostasis in cells and protects cells from iron-induced ROS. While iron is an essential component of cell processes, including mitochondrial functioning, cell proliferation and transport of oxygen, an excess of labile iron in cells can induce ferroptosis. Ferroptosis is a programmed lysosome-dependent cell death mechanism that results from iron overload, as intracellular iron ions oxidize lipids via the Fenton reaction, producing hydroxyl radicals or peroxide radicals [59]. Upregulation of FTL prevents oxidative stress and the accumulation of iron and reduces ferroptosis. The upregulation of ferritin complex proteins and the localization of DMSA-NCs within lysosomes in the EM results provides an indication that within 24 h some degradation of DMSA-NCs into iron ions within the cell had commenced. In addition, another protein involved in cellular iron recycling and regulation, HMOX1 was upregulated following DMSA-NC treatment. HMOX1 plays a cytoprotective and antioxidant role in cells either by inducing or inhibiting ferroptosis in stressed cells [60,61]. Interestingly, in a study where C17.2 neural stem cells were treated with 25 μg Fe/ml dextran-coated superparamagnetic iron oxide nanoparticles, HMOX1 expression levels similarly increased after 24 h; however, this increase was transient and reduced over the 7-day testing period [62]. Taking these results together with the lack of significant increases in ROS or superoxide production, we demonstrate that an increase of iron processing within cells following DMSA-NC treatment occurs, suggesting the initiation of degradation mechanisms within 24 h of treatment, which protect the cells from damage.

Reactome pathway and functional enrichment analysis revealed differentially expressed proteins associated with processing of capped intron-containing pre-mRNA, mRNA splicing, RNA polymerase II transcription termination and translation. As a metabolically and energetically demanding process, protein synthesis is tightly regulated during times of cellular stress to direct energy towards adaptation and maintenance of homeostasis in the face of a stressor. This response is reversible, with translation resuming to its previous rate upon the removal of the stressful stimulus. To facilitate cellular adaptability to exogenous stressors, alternative splicing and cleavage and polyadenylation processes [63] permit cells to alter their transcriptomic output by modulating gene expression during transcription, and we observed deregulation of proteins involved in these processes. Splicing of pre-mRNA is carried out by a spliceosomal complex consisting of small nuclear ribonucleoprotein particles (snRNPs) U1, U2, U4/U6 and U5, and non-snRNP protein factors [64]. Members of the snRNP family, U5 SNRNP200 and U1 SNRPC were up- and down-regulated, respectively, and U2 SF3B3 was downregulated. In addition, SRSF proteins (SRSF1, SRSF4, SRRM1 and RBM39) and hnRNPs (HNRNPU, HNRNPA2B1) were upregulated following DMSA-NC treatment. SRSF proteins hnRNPs bind to pre-mRNA and typically activate or inhibit splice site

usage, respectively, with their opposing actions contributing to the specificity of the spliceosomal machinery [65]. For instance, SRSF1 promotes the use of specific splice sites through its direct interaction with splicing factor U2AF1 [66], which is involved in the recognition of the 3′ splice site during pre-mRNA splicing. Both SRSF1 and U2AF1 were upregulated following DMSA-NC treatment. Furthermore, the U1 snRNP complex is involved in the regulation of alternative polyadenylation [67], along with other deregulated proteins including CPSF7, a subunit of the of cleavage factor CFIm, and FIP1L1, a key component of the cleavage and polyadenylation factor complex and recruited by cleavage factor Im subunit CPSF6 to enhance polyadenylation site usage [68]. Induction of alternative splicing has been demonstrated with other nanomaterials, including silver nanoparticles [69] and zinc oxide nanoparticles [70], while activation and regulation of alternative polyadenylation is influenced by increased cell proliferation [71,72], activation of neurons [73] and stressed cells [63]. Taken together, the results depict altered cellular transcription dynamics in response to DMSA-NCs and warrant further investigation to determine the extent to which gene expression is impacted.

Finally, 24 extracellular exosome proteins were deregulated (HSP90AB2P, ARF4, SLC16A1, PDCD6, RPL34, RPLP0, CACYBP, ATP1B1, RPS26, FBL, SDCBP, SPR, THRAP3, SUB1, CPD, FTH1, PSMD3, HNRNPA2B1, FLOT1, PSME2, CALR, ANP32B, LAMTOR3, FTL). Exosomes are derived from late endosomes and are exocytosed as extracellular vesicles, cellular debris or cargo to facilitate intercellular communication, and can be purified out of cells for therapeutic uses using nanotechnology (reviewed in [74]). Exosomes are involved in the transfer of ferritin-bound iron across blood–brain barrier endothelial cells and are a mechanism for transporting iron into the brain [75]. They are a potential transfer mechanism for nanoparticles between cells, as the secretion of exosomes containing inorganic nanoparticles has been demonstrated in cells previously incubated with nanoparticles for 24–48 h. This has been shown using iron oxide nanoparticles [76,77], gold nanoparticles [78] and porous silicon nanoparticles [79] across various cell types.

The deregulation of numerous proteins involved in extracellular exosomes suggests a potential externalization route for the DMSA-NC within 24 h of treatment. The blood–brain barrier is made up of three cellular layers comprising of endothelial cells, pericytes and astrocytes [80], and has long been a major obstacle in the development in diagnostic and therapeutic agents that target the brain. Further work would help determine whether DMSA-NCs are communicated between cells as exosomal cargo, permitting DMSA-NC entry into the brain via the circulatory system. Moreover, the use of exosomes in the development of treatments for diseases has received copious attention in recent times. Nanoparticles have demonstrated themselves as an excellent tool for isolating exosomes, and their large surface area allows them to be tagged with targeting ligands to improve specificity, rendering DMSA-NCs as a potentially powerful new tool in this field.

Taken together, these data support the hypothesis that at the treatment dose used in this study, DMSA-NCs are not acutely toxic to U-251 cells. The observed changes to the proteome following treatment show that DMSA-NCs induce modest perturbations to cells as they are endocytosed and transported between organelles; however, compensatory mechanisms and iron-processing mechanisms are activated. Our measures of LDH and oxidative stress demonstrated that DMSA-NC did not induce toxicity within cells, and the deregulation of spliceosomal machinery determined by proteomic analysis suggests cells maintain resilience in the face of the nanomaterials by altering their transcriptomic output. Iron-processing activity signalled that nanoparticle degradation within cells begins within 24 h. Electron microscopy demonstrated that intact nanocubes were still present at the 24-h time point; however, as DMSA-NCs degrade further, the increase of labile iron can tip the intracellular balance and induce the initiation of ferroptosis pathways. Therefore, evaluation of iron processing at later time points is essential. Degradation kinetics are important to determine because not only do they verify that nanomaterials are safely eliminated and will not accumulate in the body, they also affect the magnetization and therefore MRI contrast-enhancing ability of the nanoparticles. Therefore, these results inform future research into contrast agent delivery and imaging timescale. Furthermore, future characterization of nanoparticle–cell interactions will benefit from investigation of alternative splicing events. While it is outside of the scope of this study, splicing events are implicated in the cancer cell viability during chemotherapy. As research into nanomaterials as therapeutic delivery agents continues to increase, the results of this study can inform future development of oncotherapeutics.

While in this preliminary bioevaluation of DMSA-coated iron core iron oxide shell nanocubes we have demonstrated their potential as stable and highly biocompatible MRI T2 contrast agents, this study has several key limitations. We have shown DMSA-NC biocompatibility with U-251 glioblastoma cells; however, other cells in the body with which DMSA-NCs would interact may have differential responses. For instance, previously *in vivo* administration of iron oxide nanoparticles resulted in upregulation of autophagy and lysosomal activation in

the splenic macrophages of treated rats [81]. SH-SY5Y neurons have previously demonstrated lower uptake and susceptibility to iron oxide nanoparticle induced cytotoxicity than astrocytes [35] while other iron oxide nanoparticles induced alterations to cell apoptosis and cancer development pathways [82]. These examples demonstrate that the effect nanoparticles differs across cell types and differences in nanoparticle formulations, thus future studies must employ various biological models including different cell types, organoids and *in vivo* assessments of biocompatibility.

Furthermore, quantitative discovery proteomics identified alterations to protein expression with high accuracy and resolution. However, with the elucidation of changes to the transcription machinery, a more precise evaluation of the post-transcriptional modifications to proteins will confirm the biocompatibility of the particles, in particular with studies conducted over multiple time points. Finally, it is important to determine the precise elimination route and kinetics to ensure nanoparticles do not accumulate in tissues and result in toxicity over the long term. *In vivo* studies, investigating DMSA-coated spherical nanoparticles of a similar size, have detected nanoparticles in tissues to over 3 months postadministration [83,84] with no evidence of long-term toxicity. However, particle degradation dynamics differ between spherical and cube-shaped particles, thus it is not prudent to extrapolate these results to the present nanoparticles. Previous reports have shown the edges of cube-shaped nanoparticles are prone to enhanced biodegradation kinetics, particularly in lysosomal compartments of cells with the edges of the cubes more vulnerable than the faces [85]. Nanocubes experienced partial degradation leaving smaller, spherical particles, mostly at the endosome edges after 27 days of cellular exposure [85]. On the other hand, spherical nanoparticles coated with DMSA [83] and other coatings [85,86] have been shown to degrade particle by particle over time, with some particles remaining intact longer than others. Therefore, the next steps prior to translation of these nanoparticles to clinical settings include determining their stability and retention in an *in vivo* model.

Conclusion

In this study, we evaluated DMSA-NCs as a potential T2 MRI contrast agent. Iron-based nanocubes have been previously demonstrated to exhibit superior MRI contrast-enhancing capabilities, and for this reason are a favorable candidate for imaging. DMSA-NCs were nontoxic to U-251 glioblastoma cells and did not induce increases to reactive oxygen species, including superoxide. Furthermore, proteomics allowed determination of the protein interactions resulting in cells following exposure to DMSA-NCs. The alterations in protein profiles provided insights regarding the safety of DMSA-NCs, which contributes to the growing literature of the impacts of nanomaterials on the body. Particles that achieve higher magnetization require lower doses for sufficient contrast enhancement, mitigating the potential for adverse events in patients. The promising biocompatibility of these particles and favorable MRI contrast enhancement support the need for further development of this formulation.

Summary points

- Magnetic nanoparticles offer significant advantages in biomedical applications due to their customizable properties and biocompatibility, enhancing both therapeutics and diagnostics across various diseases.
- Superparamagnetic nanoparticles serve as effective contrast agents in MRI, enabling diagnosis of conditions such as tumors, strokes and neurodegenerative diseases by improving MRI's spatial resolution.
- Cubic-shaped magnetic nanoparticles exhibit high magnetization levels due to their high magnetic moments, low surface anisotropy and superior crystallinity, surpassing existing magnetic nanoformulations.
- Dimercaptosuccinic acid iron core iron oxide shell nanocubes (DMSA-NCs) were synthesized and proven to induce strong contrast in T2-weighted MRI.
- DMSA-NCs showed no cytotoxicity *in vitro* and did not trigger an increase in reactive oxygen species or superoxide when tested on U-251 cells, even at concentrations up to 500 μM.
- U-251 glioblastoma cells efficiently internalized DMSA-NC, with the nanocubes predominantly localizing within lysosomes and endosomes over a 24-h period.
- Proteomic analysis identified modest changes in protein expression after DMSA-NC treatment, with 56 proteins upregulated and 43 proteins downregulated in U-251 cells.
- These findings provide valuable insights into the interaction of nanoparticles with cells, particularly in terms of contrast enhancement. This contributes to the growing body of literature in nanotechnology and supports the potential for improved medical decision making.

Taylor & Francis
Taylor & Francis Group

Supplementary data

To view the supplementary data that accompany this paper please visit the journal website at: www.futuremedicine.com/doi/suppl/10.2217/nnm-2023-0304

Author contributions

The authors confirm contribution to the paper as follows: Investigation: M Ulanova, L Gloag, A Bongers, formal analysis: M Ulanova, C-K Kim; conceptualization: M Ulanova, JJ Gooding, RD Tilley, PS Sachdev, N Braidy; methodology: M Ulanova, L Gloag, HTK Duong; writing original draft: M Ulanova; writing – review and editing: M Ulanova, L Gloag, A Bongers, C-K Kim, N Braidy; funding acquisition: JJ Gooding, RD Tilley, PS Sachdev, N Braidy; supervision: JJ Gooding, RD Tilley, PS Sachdev, N Braidy.

Acknowledgments

Mass spectrometric results were obtained at the Bioanalytical Mass Spectrometry Facility within the Mark Wainwright Analytical Centre of the University of New South Wales. The authors acknowledge the facilities and the scientific and technical assistance of Microscopy Australia and of the National Imaging Facility (NIF) Australia located at the Electron Microscope Unit (EMU) and Biological Resources Imaging Laboratory (BRIL) within the Mark Wainwright Analytical Centre (MWAC) at UNSW Sydney. Parts of the figures were drawn by using pictures from Bioicons, specifically, transmission-electron-microscope-tem icon, microtube-closed icon, and plate-reader icon by DBCLS https://togotv.dbcls.jp/en/pics.html is licensed under CC-BY 4.0 Unported https://creativecommons.org/licenses/by/4.0/.

Financial disclosure

The authors acknowledge funding under the Australian Research Council Discovery Project (RD Tilley, DP190102659 and RD Tilley and A Bongers DP200100143) and National Health and Medical Research Council (NHMRC) Investigator Grant (JJ Gooding, GNT1196648). N Braidy is a recipient of the Australian Research Council Discovery Early Career Award (DE170100628). N Braidy and PS Sachdev acknowledge funding from Yulgibar Foundation and Dementia Australia. PS Sachdev acknowledges NHMRC funding through an Investigator Leadership grant. M Ulanova was a recipient of the Australian Postgraduate Award PhD scholarship. C-K Kim in a recipient of the University of New South Wales University International Postgraduate Award (UIPA) scholarship. The authors have no other relevant affiliations or financial involvement with any organization or entity with a financial interest in or financial conflict with the subject matter or materials discussed in the manuscript apart from those disclosed.

Competing interests disclosure

PS Sachdev was member of Advisory Committee for Biogen Australia and Roche Australia in 2020–2021. The authors have no other competing interests or relevant affiliations with any organization or entity with the subject matter or materials discussed in the manuscript apart from those disclosed.

Writing disclosure

No writing assistance was utilized in the production of this manuscript.

References

Papers of special note have been highlighted as: • of interest

1. Xiao Y, Gong W, Zhao M, Zhang M, Lu N. Surface-engineered prussian blue nanozymes as artificial receptors for universal pattern recognition of metal ions and proteins. *Sens. Actuat. B. Chem.* 390, 134006 (2023).
2. Tian R, Li Y, Xu Z, Xu J, Liu J. Current advances of atomically dispersed metal-centered nanozymes for tumor diagnosis and therapy. *Int. J. Mol. Sci.* 24(21), 15712 (2023).
3. Hajinezhad MR, Shahraki S, Nikfarjam Z *et al.* Development of a new vesicular formulation for delivery of ifosfamide: evidence from *in vitro*, *in vivo*, and *in silico* experiments. *Arab. J. Chem.* 16(9), 105086 (2023).
4. McGrath AJ, Dolan C, Cheong S *et al.* Stability of polyelectrolyte-coated iron nanoparticles for T2-weighted magnetic resonance imaging. *J. Magn. Magn.* 439, 251–258 (2017).

• **Synthesis and characterization of custom-synthesized phosphonate-grafted polyelectrolytes (PolyM3) of various chain lengths, for efficient coating of iron nanoparticles with a native iron oxide shell.**

5. Cheong S, Ferguson P, Feindel KW *et al.* Simple synthesis and functionalization of iron nanoparticles for magnetic resonance imaging. *Angew. Chem. Int. Ed.* 50(18), 4206–4209 (2011).

• **Synthesis of single-crystal core/shell iron/iron oxide nanoparticles which are highly effective magnetic resonance imaging contrast agents to detect small tumors.**

6. Herman DA, Ferguson P, Cheong S *et al.* Hot-injection synthesis of iron/iron oxide core/shell nanoparticles for T2 contrast enhancement in magnetic resonance imaging. *Chem. Commun. (Camb.)* 47(32), 9221–9223 (2011).
7. Zhen G, Muir BW, Moffat BA *et al.* Comparative study of the magnetic behavior of spherical and cubic superparamagnetic iron oxide nanoparticles. *J. Phys. Chem. C.* 115(2), 327–334 (2011).
8. Gulzar A, Ayoub N, Mir JF, Alanazi AM, Shah MA, Gulzar A. *In vitro* and *in vivo* MRI imaging and photothermal therapeutic properties of hematite (α-Fe_2O_3) nanorods. *J. Mat. Sci. Mat. Med.* 33(1), 10 (2022).
9. Avolio M, Gavilán H, Mazario E *et al.* Elongated magnetic nanoparticles with high-aspect ratio: a nuclear relaxation and specific absorption rate investigation. *Phys. Chem. Chem. Phys.* 21(34), 18741–18752 (2019).
10. Rehman ZU, Iqbal MZ, Hou J *et al.* Graphitic carbon nitride–manganese oxide nanoflowers as promising T1 magnetic resonance imaging contrast material. *Appl. Phys. A.* 128(10), 926 (2022).
11. McKiernan EP, Moloney C, Roy Chaudhuri T *et al.* Formation of hydrated PEG layers on magnetic iron oxide nanoflowers shows internal magnetisation dynamics and generates high *in-vivo* efficacy for MRI and magnetic hyperthermia. *Acta Biomater.* 152, 393–405 (2022).
12. Thomas G, Boudon J, Maurizi L *et al.* Innovative magnetic nanoparticles for PET/MRI bimodal imaging. *ACS Omega* 4(2), 2637–2648 (2019).
13. Guardia P, Di Corato R, Lartigue L *et al.* Water-soluble iron oxide nanocubes with high values of specific absorption rate for cancer cell hyperthermia treatment. *ACS Nano.* 6(4), 3080–3091 (2012).
14. Salazar-Alvarez G, Qin J, Šepelák V *et al.* Cubic versus spherical magnetic nanoparticles: the role of surface anisotropy. *J. Am. Chem. Soc.* 130(40), 13234–13239 (2008).
15. Khurshid H, Alonso J, Nemati Z *et al.* Anisotropy effects in magnetic hyperthermia: a comparison between spherical and cubic exchange-coupled FeO/Fe_3O_4 nanoparticles. *J. Appl. Phys.* 117(17), 17A337 (2015).
16. Naumenko V, Garanina A, Nikitin A *et al.* Biodistribution and tumors MRI contrast enhancement of magnetic nanocubes, nanoclusters, and nanorods in multiple mice models. *Contrast Media Mol.* 2018, 8264208 (2018).
17. Cho HR, Choi SH, Lee N, Hyeon T, Kim H, Moon WK. Macrophages homing to metastatic lymph nodes can be monitored with ultrasensitive ferromagnetic iron-oxide nanocubes and a 1.5T clinical MR scanner. *PLOS ONE* 7(1), e29575 (2012).
18. Choo P, Liu T, Odom TW. Nanoparticle shape determines dynamics of targeting nanoconstructs on cell membranes. *J. Am. Chem. Soc.* 143(12), 4550–4555 (2021).
19. Wang W, Gaus K, Tilley RD, Gooding JJ. The impact of nanoparticle shape on cellular internalisation and transport: what do the different analysis methods tell us? *Mater. Horiz.* 6(8), 1538–1547 (2019).
20. Lee JH, Ju JE, Kim BI *et al.* Rod-shaped iron oxide nanoparticles are more toxic than sphere-shaped nanoparticles to murine macrophage cells. *Environ. Toxicol. Chem.* 33(12), 2759–2766 (2014).
21. Ispas C, Andreescu D, Patel A, Goia DV, Andreescu S, Wallace KN. Toxicity and developmental defects of different sizes and shape nickel nanoparticles in zebrafish. *Environ. Sci. Technol.* 43(16), 6349–6356 (2009).
22. Stoehr LC, Gonzalez E, Stampfl A *et al.* Shape matters: effects of silver nanospheres and wires on human alveolar epithelial cells. *Part. Fibre Toxicol.* 8, 36–36 (2011).
23. Çitoğlu S, Coşkun ÖD, Tung LD, Onur MA, Thanh NTK. DMSA-coated cubic iron oxide nanoparticles as potential therapeutic agents. *Nanomedicine* 16(11), 925–941 (2021).
24. Qin M, Peng Y, Xu M *et al.* Uniform Fe_3O_4/Gd_2O_3-DHCA nanocubes for dual-mode magnetic resonance imaging. *Beilstein. J. Nanotech.* 11, 1000–1009 (2020).
25. Pardo A, Yáñez S, Piñeiro Y *et al.* Cubic anisotropic Co- and Zn-substituted ferrite nanoparticles as multimodal magnetic agents. *ACS Appl. Mater. Interfaces* 12(8), 9017–9031 (2020).
26. Wu Y, Lu Z, Li Y, Yang J, Zhang X. Surface modification of iron oxide-based magnetic nanoparticles for cerebral theranostics: application and prospection. *Nanomaterials (Basel)* 10(8), 1441 (2020).
27. Ulanova M, Poljak A, Wen W *et al.* Nanoparticles as contrast agents for the diagnosis of Alzheimer's disease: a systematic review. *Nanomedicine* 15(7), 725–743 (2020).
28. Ulanova M, Gloag L, Bongers A *et al.* Evaluation of dimercaptosuccinic acid-coated iron nanoparticles immunotargeted to amyloid beta as MRI contrast agents for the diagnosis of Alzheimer's disease. *Cells* 12(18), (2023).

• **Shows the potential of implementing iron-based nanomaterials as tools for early Alzheimer's disease diagnosis.**

29. Mousa AH, Mohammad SA. Potential role of chitosan, PLGA and iron oxide nanoparticles in Parkinson's disease therapy. *Egypt J. Neurol. Psychiatr. Neurosurg.* 58(1), 68 (2022).

30. Israel LL, Galstyan A, Holler E, Ljubimova JY. Magnetic iron oxide nanoparticles for imaging, targeting and treatment of primary and metastatic tumors of the brain. *J. Control. Rel.* 320, 45–62 (2020).
31. Dai D, He L, Chen Y, Zhang C. Astrocyte responses to nanomaterials: functional changes, pathological changes and potential applications. *Acta Biomater.* 122, 66–81 (2021).
32. Geppert M, Hohnholt MC, Thiel K *et al.* Uptake of dimercaptosuccinate-coated magnetic iron oxide nanoparticles by cultured brain astrocytes. *Nanotechnology* 22(14), 145101 (2011).
33. Hawkins SJ, Crompton LA, Sood A *et al.* Nanoparticle-induced neuronal toxicity across placental barriers is mediated by autophagy and dependent on astrocytes. *Nat. Nanotechnol.* 13(5), 427–433 (2018).
34. Limón-Pacheco JH, Jiménez-Barrios N, Déciga-Alcaraz A *et al.* Astrocytes are more vulnerable than neurons to silicon dioxide nanoparticle toxicity *in vitro*. *Toxics* 8(3), 51 (2020).
35. Coccini T, Caloni F, Ramírez Cando LJ, De Simone U. Cytotoxicity and proliferative capacity impairment induced on human brain cell cultures after short- and long-term exposure to magnetite nanoparticles. *J. Appl. Toxicol.* 37(3), 361–373 (2017).
36. Schneider CA, Rasband WS, Eliceiri KW. NIH Image to ImageJ: 25 years of image analysis. *Nat. Methods* 9(7), 671–675 (2012).
37. Kaur G, Poljak A, Ali SA, Zhong L, Raftery MJ, Sachdev P. Extending the depth of human plasma proteome coverage using simple fractionation techniques. *J. Proteome Res.* 20(2), 1261–1279 (2021).
38. Tyanova S, Temu T, Sinitcyn P *et al.* The Perseus computational platform for comprehensive analysis of (prote)omics data. *Nat. Methods* 13(9), 731–740 (2016).
39. Wu T, Hu E, Xu S *et al.* clusterProfiler 4.0: A universal enrichment tool for interpreting omics data. *Innovation (Camb.)* 2(3), 100141 (2021).
40. Yu G, He QY. ReactomePA: an R/Bioconductor package for Reactome pathway analysis and visualization. *Mol. Biosyst.* 12(2), 477–479 (2016).
41. Szklarczyk D, Gable AL, Nastou KC *et al.* The STRING database in 2021: customizable protein-protein networks, and functional characterization of user-uploaded gene/measurement sets. *Nucleic Acids Res.* 49(D1), D605–d612 (2021).
42. Gloag L, Mehdipour M, Ulanova M *et al.* Zero valent iron core-iron oxide shell nanoparticles as small magnetic particle imaging tracers. *ChemComm (Camb.)* 56(24), 3504–3507 (2020).

- **Includes further chemical characterization of iron core iron oxide shell nanoparticles.**

43. Sherman BT, Hao M, Qiu J *et al.* DAVID: a web server for functional enrichment analysis and functional annotation of gene lists (2021 update). *Nucleic Acids Res.* DOI: 10.1093/nar/gkac194 (2022).
44. Huang DW, Sherman BT, Lempicki RA. Systematic and integrative analysis of large gene lists using DAVID bioinformatics resources. *Nat. Protoc.* 4(1), 44–57 (2009).
45. Naha PC, Chhour P, Cormode DP. Systematic in vitro toxicological screening of gold nanoparticles designed for nanomedicine applications. *Toxicol. In Vitro* 29(7), 1445–1453 (2015).
46. Shannahan JH, Lai X, Ke PC, Podila R, Brown JM, Witzmann FA. Silver nanoparticle protein corona composition in cell culture media. *PLOS ONE* 8(9), e74001–e74001 (2013).
47. Wiogo HT, Lim M, Bulmus V, Yun J, Amal R. Stabilization of magnetic iron oxide nanoparticles in biological media by fetal bovine serum (FBS). *Langmuir* 27(2), 843–850 (2011).
48. Amiri H, Bordonali L, Lascialfari A *et al.* Protein corona affects the relaxivity and MRI contrast efficiency of magnetic nanoparticles. *Nanoscale* 5(18), 8656–8665 (2013).
49. Lee N, Choi Y, Lee Y *et al.* Water-dispersible ferrimagnetic iron oxide nanocubes with extremely high r2 relaxivity for highly sensitive *in vivo* MRI of tumors. *Nano. Lett.* 12(6), 3127–3131 (2012).
50. Bae KH, Park M, Do MJ *et al.* Chitosan oligosaccharide-stabilized ferrimagnetic iron oxide nanocubes for magnetically modulated cancer hyperthermia. *ACS Nano.* 6(6), 5266–5273 (2012).
51. Sharma VK, Alipour A, Soran-Erdem Z, Aykut ZG, Demir HV. Highly monodisperse low-magnetization magnetite nanocubes as simultaneous T(1)–T(2) MRI contrast agents. *Nanoscale* 7(23), 10519–10526 (2015).
52. Silvestri N, Gavilán H, Guardia P *et al.* Di- and tri-component spinel ferrite nanocubes: synthesis and their comparative characterization for theranostic applications. *Nanoscale* 13(32), 13665–13680 (2021).
53. Luther EM, Petters C, Bulcke F *et al.* Endocytotic uptake of iron oxide nanoparticles by cultured brain microglial cells. *Acta Biomater.* 9(9), 8454–8465 (2013).
54. Levada K, Pshenichnikov S, Omelyanchik A *et al.* Progressive lysosomal membrane permeabilization induced by iron oxide nanoparticles drives hepatic cell autophagy and apoptosis. *Nano Converg.* 7(1), 17–17 (2020).
55. Serda RE, Mack A, van de Ven AL *et al.* Logic-embedded vectors for intracellular partitioning, endosomal escape, and exocytosis of nanoparticles. *Small* 6(23), 2691–2700 (2010).
56. Abu-Bakr AF, Zubarev AY. Effect of ring-shaped clusters on magnetic hyperthermia: modelling approach. *Philos. Trans. Royal Soc. A.* 379(2205), 20200316 (2021).

57. Luo T, Gao J, Lin N, Wang J. Effects of two kinds of iron nanoparticles as reactive oxygen species inducer and scavenger on the transcriptomic profiles of two human leukemia cells with different stemness. *Nanomaterials* 10(10), 1951 (2020).
58. Xie Y, Jiang J, Tang Q *et al.* Iron oxide nanoparticles as autophagy intervention agents suppress hepatoma growth by enhancing tumoricidal autophagy. *Adv. Sci.* 7(16), 1903323 (2020).
59. Ngoka LCM. Dramatic down-regulation of oxidoreductases in human hepatocellular carcinoma hepG2 cells: proteomics and gene ontology unveiling new frontiers in cancer enzymology. *Proteome Sci.* 6(1), 29 (2008).
60. Kwon MY, Park E, Lee SJ, Chung SW. Heme oxygenase-1 accelerates erastin-induced ferroptotic cell death. *Oncotarget* 6(27), 24393–24403 (2015).
61. Adedoyin O, Boddu R, Traylor A *et al.* Heme oxygenase-1 mitigates ferroptosis in renal proximal tubule cells. *Am. J. Physiol. Renal. Physiol.* 314(5), F702–F714 (2017).
62. Kedziorek DA, Muja N, Walczak P *et al.* Gene expression profiling reveals early cellular responses to intracellular magnetic labeling with superparamagnetic iron oxide nanoparticles. *Magn. Reson. Med.* 63(4), 1031–1043 (2010).
63. Hollerer I, Curk T, Haase B *et al.* The differential expression of alternatively polyadenylated transcripts is a common stress-induced response mechanism that modulates mammalian mRNA expression in a quantitative and qualitative fashion. *RNA* 22(9), 1441–1453 (2016).
64. Gallego-Paez LM, Bordone MC, Leote AC, Saraiva-Agostinho N, Ascensão-Ferreira M, Barbosa-Morais NL. Alternative splicing: the pledge, the turn, and the prestige: the key role of alternative splicing in human biological systems. *Hum. Genet.* 136(9), 1015–1042 (2017).
65. Busch A, Hertel KJ. Evolution of SR protein and hnRNP splicing regulatory factors. *Wiley Interdiscip. Rev. RNA* 3(1), 1–12 (2012).
66. Wu JY, Maniatis T. Specific interactions between proteins implicated in splice site selection and regulated alternative splicing. *Cell* 75(6), 1061–1070 (1993).
67. Kaida D. The reciprocal regulation between splicing and 3′-end processing. *Wiley Interdiscip. Rev. RNA* 7(4), 499–511 (2016).
68. Hu Z, Li M, Huo Z *et al.* U1 snRNP proteins promote proximal alternative polyadenylation sites by directly interacting with 3′ end processing core factors. *J. Mol. Cell Biol.* 14(8), mjac054 (2022).
69. Bozhko IV, Minchenko DO, Zinchenko TO, Iavorovskĭ OP, Minchenko OG. [Effect of silver nanoparticles on the expression of 6-phosphofructo-2-kinase/fructose-2,6-bisphosphatase-2 mRNA and its alternative splice variants in different rat organs]. *Ukr. Biokhim. Zh. (1999)* 82(5), 68–78 (2010).
70. Rossner P, Vrbova K, Strapacova S *et al.* Inhalation of ZnO nanoparticles: splice junction expression and alternative splicing in mice. *Toxicol. Sci.* 168(1), 190–200 (2019).
71. Elkon R, Drost J, van Haaften G *et al.* E2F mediates enhanced alternative polyadenylation in proliferation. *Genome Biol.* 13(7), R59 (2012).
72. Sandberg R, Neilson JR, Sarma A, Sharp PA, Burge CB. Proliferating cells express mRNAs with shortened 3′ untranslated regions and fewer microRNA target sites. *Science* 320(5883), 1643–1647 (2008).
73. Flavell SW, Kim TK, Gray JM *et al.* Genome-wide analysis of MEF2 transcriptional program reveals synaptic target genes and neuronal activity-dependent polyadenylation site selection. *Neuron* 60(6), 1022–1038 (2008).
74. Wang Y, Wang W, Kong F *et al.* Tango of dual nanoparticles: interplays between exosomes and nanomedicine. *Bioeng. Transl. Med.* 7(2), e10269 (2022).
75. Palsa K, Baringer SL, Shenoy G, Spiegelman VS, Simpson IA, Connor JR. Exosomes are involved in iron transport from human blood–brain barrier endothelial cells and are modified by endothelial cell iron status. *J. Biol. Chem.* 299(2), 102868 (2023).
76. Jung KO, Jo H, Yu JH, Gambhir SS, Pratx G. Development and MPI tracking of novel hypoxia-targeted theranostic exosomes. *Biomaterials* 177, 139–148 (2018).
77. Lee JR, Park BW, Kim J *et al.* Nanovesicles derived from iron oxide nanoparticles-incorporated mesenchymal stem cells for cardiac repair. *Sci. Adv.* 6(18), eaaz0952 (2020).
78. Lara P, Palma-Florez S, Salas-Huenuleo E *et al.* Gold nanoparticle based double-labeling of melanoma extracellular vesicles to determine the specificity of uptake by cells and preferential accumulation in small metastatic lung tumors. *J. Nanobiotechnol.* 18(1), 20 (2020).
79. Yong T, Zhang X, Bie N *et al.* Tumor exosome-based nanoparticles are efficient drug carriers for chemotherapy. *Nat. Commun.* 10(1), 3838 (2019).
80. Kadry H, Noorani B, Cucullo L. A blood–brain barrier overview on structure, function, impairment, and biomarkers of integrity. *Fluids Barriers CNS* 17(1), 69 (2020).
81. Han J, Tian Y, Wang M *et al.* Proteomics unite traditional toxicological assessment methods to evaluate the toxicity of iron oxide nanoparticles. *Front. Pharmacol.* 13, 1011065 (2022).
82. Askri D, Cunin V, Béal D *et al.* Investigating the toxic effects induced by iron oxide nanoparticles on neuroblastoma cell line: an integrative study combining cytotoxic, genotoxic and proteomic tools. *Nanotoxicology* 13(8), 1021–1040 (2019).

- **Interesting study implementing an integrated -omics approach for investigation of iron oxide nanoparticles impacts on neuroblastoma cells.**

83. Portilla Y, Fernández-Afonso Y, Pérez-Yagüe S *et al.* Different coatings on magnetic nanoparticles dictate their degradation kinetics *in vivo* for 15 months after intravenous administration in mice. *J. Nanobiotechnol.* 20(1), 543 (2022).
84. Mejías R, Gutiérrez L, Salas G *et al.* Long term biotransformation and toxicity of dimercaptosuccinic acid-coated magnetic nanoparticles support their use in biomedical applications. *J. Control. Rel.* 171(2), 225–233 (2013).
85. Mazuel F, Espinosa A, Luciani N *et al.* Massive intracellular biodegradation of iron oxide nanoparticles evidenced magnetically at single-endosome and tissue levels. *ACS Nano* 10(8), 7627–7638 (2016).
86. Lévy M, Lagarde F, Maraloiu V-A *et al.* Degradability of superparamagnetic nanoparticles in a model of intracellular environment: follow-up of magnetic, structural and chemical properties. *Nanotechnology* 21(39), 395103 (2010).